A model intercomparison of Titan's climate and low-latitude environment

Juan Lora, Tetsuya Tokano, Jan Vatant D'ollone, Sébastien Lebonnois, Ralph Lorenz

To cite this version:

Juan Lora, Tetsuya Tokano, Jan Vatant D'ollone, Sébastien Lebonnois, Ralph Lorenz. A model intercomparison of Titan's climate and low-latitude environment. Icarus, 2019, 333, pp.113-126. 10.1016/j.icarus.2019.05.031 . hal-02323559

HAL Id: hal-02323559
https://hal.science/hal-02323559v1

Submitted on 4 Dec 2023

A model intercomparison of Titan's climate and low-latitude environment

Juan M. Lora[a,b], Tetsuya Tokano[c], Jan Vatant d'Ollone[d],
Sébastien Lebonnois[d], Ralph D. Lorenz[e]

[a] *Department of Earth, Planetary and Space Sciences, University of California, Los Angeles, California, USA*
[b] *Department of Geology and Geophysics, Yale University, New Haven, Connecticut, USA*
[c] *Institut für Geophysik und Meteorologie, Universität zu Köln, Köln, Germany*
[d] *Laboratoire de Météorologie Dynamique, IPSL, CNRS/UPMC, Paris, France*
[e] *Johns Hopkins Applied Physics Laboratory, Laurel, Maryland, USA*

Abstract

Cassini-Huygens provided a wealth of data with which to constrain numerical models of Titan. Such models have been employed over the last decade to investigate various aspects of Titan's atmosphere and climate, and several three-dimensional general circulation models (GCMs) now exist that simulate Titan with a high degree of fidelity. However, substantial uncertainties persist, and at the same time no dedicated intercomparisons have assessed the degree to which these models agree with each other or the observations. To address this gap, and motivated by the proposed Dragonfly Titan lander mission, we directly compare three Titan GCMs to each other and to *in situ* observations, and also provide multi-model expectations for the low-latitude environment during the early northern winter season. Globally, the models qualitatively agree in their representation of the atmospheric circulation and structure, though one model severely underestimates

---

Email address: `juan.lora@yale.edu` (Juan M. Lora)

zonal winds and latitudinal temperature gradients. We find that, at low latitudes, simulated and observed atmospheric temperatures closely agree in all cases, while the measured winds above the boundary layer are only quantitatively matched by one model. Nevertheless, the models simulate similar near-surface winds, and all indicate these are weak. Likewise, temperatures and methane content at low latitudes are similar between models, with some differences that are largely attributable to modeling assumptions. All models predict environments that closely resemble that encountered by the Huygens probe, including little or no precipitation at low latitudes during northern winter. The most significant differences concern the methane cycle, though the models are least comparable in this area and substantial uncertainties remain. We suggest that, while the overall low-latitude environment on Titan at this season is now fairly well constrained, future *in situ* measurements and monitoring will transform our understanding of regional and temporal variability, atmosphere-surface coupling, Titan's methane cycle, and modeling thereof.

Keywords: Titan, Climate, Atmospheres, Meteorology

---

1. Introduction

The Cassini-Huygens mission transformed our understanding of Titan, clarifying many aspects of its climate system but also leaving tantalizing unanswered questions. Remote sensing observations, building on prior and ongoing ground-based efforts, revealed a perplexing scarcity of tropospheric methane clouds, but also demonstrated the existence of strong seasonal evolution and the occurrence of precipitation (Turtle et al., 2011a,c; Rodriguez et al., 2011; Turtle et al., 2018b). Lakes and seas, as well as flooded canyons, empty lake beds, and dry channels were discovered on Titan's surface, along with vast expanses of equatorial dunes (Tomasko et al., 2005; Lorenz et al., 2006b; Stofan et al., 2007; Hayes et al., 2008; Radebaugh et al., 2008; Hayes, 2016; Poggiali et al., 2016) that together point to a complex, dichotomous, latitudinally-dependent climate (Mitchell and Lora, 2016). Yet despite these advances, the nature of the connection between (sub)surface and atmosphere remains elusive (Mitchell and Lora, 2016; Turtle et al., 2018b).

Huygens also provided the first *in situ* measurements of Titan, yielding estimates of winds and measurements of temperatures from inside the atmosphere at unprecedented precision, along with determination of the composition of the lower atmosphere (Bird et al., 2005; Fulchignoni et al., 2005; Niemann et al., 2005; Niemann et al., 2010; Karkoschka, 2016). But data from Huygens covered only one location during a single entry, and we still have no direct measurement of the surface composition. Similarly, though the Huygens temperature profile provided an invaluable confirmation of retrieved temperatures from other methods (Lindal et al., 1983; Schinder et al., 2011), information on the variability of the atmosphere on diurnal and synoptic time scales is still lacking. These gaps prevent a full comprehension of Titan's meteorology, though modeling has helped to constrain our ignorance.

The increasing quality and complexity of data from Titan has motivated the development and application of numerous general circulation models (GCMs), with which many aspects of Titan's climate system have been interpreted or inferred. Examples include the atmospheric superrotation, the circulation and chemistry of the middle atmosphere, the tropospheric methane cycle, the interactions of surface and atmosphere, as well as Titan's paleoclimate. But these studies have largely been carried out with independent models (which also range considerably in complexity), and little attempt has been made to understand or account for potential model biases or structural differences, so many results may yet prove to be model-dependent.

Therefore, the purpose of this work is twofold: To synthesize and compare detailed climate modeling results for Titan's low-latitude climate, benchmarked where possible by the *in situ* data, and at the same time to provide context and expectations, based on multi-model results, for the Titan environment at the time of arrival of the proposed Dragonfly rotorcraft lander. The Dragonfly mission concept (Lorenz et al., 2018; Turtle et al., 2018a) would represent a dramatic follow-up *in situ* investigation of Titan to Huygens, enabling, among other things, atmospheric measurements and environmental monitoring to improve our understanding of meteorology and the methane cycle, and provide heretofore unparalleled constraints for climate models. A thorough synthesis of the state of knowledge concerning Titan climate models is thus a timely need.

Model intercomparison exercises have a long history. They have been a major focus of the international Earth climate community over the past two decades, most recently through the sixth phase of the Climate Model Intercomparison Project (CMIP6; Eyring et al., 2016). In the context of planetary climates, intercomparisons have also been carried out for Mars and Venus (e.g., Lebonnois et al., 2013). But despite a relative wealth of Titan GCMs, only very limited multi-model work or comparisons have been attempted (Lorenz et al., 2012; Hayes et al., 2013; Griffith et al., 2014; Mc-

Donald et al., 2016), and benchmarking of simulations has been mixed. This is particularly important for more complex models that attempt to simulate Titan's climate with high fidelity, as mechanistic understanding is more difficult in such cases and extended parameter explorations are impracticable. Therefore, here we attempt a detailed intercomparison of Titan GCMs, and obtain some high-level conclusions.

2. Models and Methodology

This paper presents an intercomparison of three general circulation models (GCMs) of Titan's atmosphere, focusing in particular on the low latitudes during the time following northern winter solstice, which is roughly equivalent to the month of January on Earth. This region and time are chosen because they correspond to the location and date of the descent of the Huygens probe through Titan's atmosphere in 2005, as well as to the arrival of the proposed Dragonfly mission around 2034, almost exactly one Titan year later. We focus specifically on the lower atmospheric and surface environment, and compare the models' climatological predictions for basic characteristics like winds, temperatures, methane content, and, where possible, precipitation.

Three models are involved in this intercomparison, all of which are fully three-dimensional and simulate the low to middle atmosphere of Titan; these models have been widely used and are extensively documented in the literature (see Lebonnois et al., 2012; Lora et al., 2015; Tokano, 2019). Very brief overviews of the models are given in the following subsection and in Table 1. A fourth model, TitanWRF (Newman et al., 2016), was also invited but was unable to participate.

Table 1: Titan GCMs used in this study

Model Name (Abbr.)	Resolution (lon×lat)	Topography	Methane Cycle	Moist Convection	Titan Years Run	Reference
IPSL Titan GCM (IPSL)	64×48	Yes	No[a]	No	10	Lebonnois et al. (2012)
Cologne Titan GCM (Köln)	32×24	Yes	Yes[b]	No	10	Tokano (2019)
Titan Atmospheric Model (TAM)	64×32	No	Yes[b]	Yes	20	Lora et al. (2015)

[a] Surface methane mole fraction is forced to 0.0565 (Niemann et al., 2010).

[b] Surface hydrology is treated with a simple bucket scheme.

The models used in this study represent some of the highest-fidelity simulations of Titan's climate, and are the most comprehensive Titan atmospheric models available, though relative to Earth GCMs they can at most be considered models of intermediate complexity (as opposed to fully coupled climate models or Earth system models). Other modeling frameworks have been extensively used to study various aspects of Titan's climate or atmosphere—particularly using two-dimensional or axisymmetric domains (e.g., Mitchell et al., 2006; Rannou et al., 2006; Crespin et al., 2008) and/or simpler or more idealized configurations (e.g., Mitchell et al., 2011; Schneider et al., 2012)—but in this context we are most interested in models that attempt to simulate Titan's lower atmosphere with the highest level of realism.

2.1. Model descriptions

The Institut Pierre Simon Laplace Titan GCM (henceforth the IPSL model) uses the finite-difference dynamical core of the Laboratoire de Météorologie Dynamique (LMDZ5), with physical parameterizations for soil temperatures, surface–atmosphere fluxes and turbulent diffusion, as well as Saturn's gravitational tide (see Lebonnois et al., 2012). The radiative transfer parameterization, previously based on the model of McKay et al. (1989), has been updated with a multiple-scattering code that employs correlated k-coefficients, with a fixed vertical profile of haze opacity (Lavvas et al., 2010). A fixed methane profile (Niemann et al., 2010) is used in the radiative transfer, and the model does not fully simulate the methane cycle; instead, the surface-level methane mole fraction is held constant everywhere, at a value of 0.0565 based on Niemann et al. (2010). The model uses the topography map of Lorenz et al. (2013).

The University of Cologne (Köln) Titan GCM, henceforth the Köln model, uses the grid-point dynamical core of the Aries/Geos GCM, updated to be quasi-hydrostatic (Tokano, 2013). It parameterizes surface temperatures, methane condensation, and surface–atmosphere fluxes with a moisture availability parameter of 0.5, as well as Saturn's gravitational tide. A simple bucket scheme is used for hydrology. For radiative transfer, the model uses the scheme of McKay et al. (1989) with a multiplicative correction factor to tune the heating/cooling rates to observed values (Tomasko et al., 2008c); this guarantees accurate low-latitude temperatures, though the model greatly underestimates latitudinal temperature gradients (Sec. 3.2; Tokano, 2019). Topography based on the map of Lorenz et al. (2013) is included.

The Titan Atmospheric Model (TAM) uses the GFDL Flexible Modeling System and employs the FMS spectral dynamical core plus component modules to parameterize unresolved physical processes. These include schemes to compute moist processes, including convection, condensation, and precipitation of methane; surface and ground temperatures; surface–atmosphere fluxes and turbulent diffusion; and full radiative transfer that uses a combination of Cassini measurements (Tomasko et al., 2008a,b) and correlated k-coefficients (see Lora et al., 2015). Saturn's gravitational tide is not parameterized. The model employs a simple bucket scheme for hydrology, and is run in a configuration with imposed surface methane at high latitudes and liquid infiltration at low latitudes, which has been shown to reproduce a number of observations of Titan's hydroclimate (Lora and Mitchell, 2015; Mitchell and Lora, 2016; Lora and Ádámkovics, 2017; Faulk et al., 2017).

2.2. Methodology

Multi-year simulations were run for all models (see Table 1) in order to incorporate interannual variability. Due to the length of Titan years (29.5 Earth years) combined with the models' high temporal resolution, recording simulation results for every variable at every time step was impossible. Therefore, we opted to save the average, maximum, and minimum of each desired variable (at every model layer, where applicable) for each Titan day (Tsol), allowing us to quantify the full range of diurnal to interannual variability but limiting the temporal resolution of the output. In addition to the multi-year runs, a subset of additional short (10 Tsol) simulations were run with sufficiently high output frequency to resolve diurnal variations (see Sec. 5.3).

Each model was run in the configuration available and preferred by its authors. Therefore, not all models fully simulate the methane cycle, and in each case the surface methane reservoir is treated differently; only two models include the effects of topography, and only one model parameterizes moist convection. These substantial differences imply that not all comparisons are equal (or possible), though perhaps model agreement therefore suggests robustness. Nevertheless, this work represents the first dedicated intercomparison of Titan GCMs, and we consider the cataloguing of major discrepancies and areas of resemblance an important step toward characterizing the state of the field.

3. Global context

Though our focus in this paper is the low-latitude environment, we begin by comparing the general circulation and atmospheric structure of the lower atmosphere as simulated by the three models, to provide a global context. Figs. 1 and 2 show the zonal-mean zonal winds alongside meridional mass streamfunctions and the zonal-mean temperatures for two contrasting times of year, northern winter solstice ($L_S = 270°$) and northern vernal equinox ($L_S = 0°$).

3.1. Circulation

The zonal winds simulated by the IPSL model increase from the surface to lower atmospheric pressures at all latitudes, with particularly strong flows concentrated around low latitudes that are a clear indication of substantial superrotation (Fig. 1a,d). There is a local maximum in wind speed around 50 hPa and a region of lower speeds around 25 hPa that corresponds to the low-latitude profile measured by the Huygens probe (Bird et al., 2005). There is a slight latitudinal asymmetry in the winds at northern winter solstice (Fig. 1a), which intensifies at the northern vernal equinox as peak wind speeds shift northward (Fig. 1d).

The corresponding mean meridional circulation shows a near-global solsticial Hadley cell at higher pressures, and a thermally indirect cell at the pressures of the zonal wind local minimum. The circulation at equinox is more complicated and shows considerable structure. In both hemispheres, a direct circulation is apparent up to high latitudes, but punctuated by confined regions of indirect flow. At lower pressures, the circulation is dominantly clockwise, except at mid-northern latitudes where it reverses. Thus, the meridional circulation in the lower atmosphere is separated from that of upper levels. The latitudinal structure visible at higher pressures is due to the presence of topography in this model; this is numerical noise that likely does not accurately represent Titan, though its effects on momentum transport and the superrotation are likely not significant (as seen in the zonal winds).

The Köln model's zonal winds are much lower in magnitude throughout the atmosphere for both seasons, and do not show superrotation (Fig. 1b,e). This model's inability to reproduce Titan's superrotating zonal circulation has been noted since its inception (Tokano et al., 1999), and represents an important deficiency. At higher latitudes (around 60° in the northern hemisphere), wind speeds are slightly higher, but still do not reach 10 m s^{-1}.

On the other hand, the meridional circulation simulated by the Köln model is much smoother than in the IPSL model, despite its also including topography. At the solstice, there is a clear, global Hadley cell extending from pole to pole and throughout the lower atmosphere (Fig. 1b), with a small region of counterclockwise flow near the surface at mid-southern latitudes. The values of the mass streamfunction are similar to the IPSL model's around 100 hPa. At the equinox, the circulation shows two highly symmetric direct cells, indicating rising motion precisely at the equator, with poleward flow aloft (Fig. 1e).

The zonal winds simulated by TAM increase strongly with height through the lower atmosphere, and reach values larger than 50 m s^{-1} at pressures above 10 hPa at all latitudes equatorward of 60°, clearly showing robust superrotation (Fig. 1c,f). Strong westerly winds extend closer to the surface at higher latitudes. The solstitial winds are largely latitudinally symmetric (Fig. 1c), and, as in the IPSL model simulation, peak winds shift northward at equinox (Fig. 1f).

The meridional circulation simulated by TAM is very similar to that from the Köln model, with some small differences. At solstice, a global Hadley cell extends from south pole to high northern latitudes, but there is a near-surface region of indirect circulation over the northern pole (Fig. 1f). Similarly, roughly latitudinally symmetric direct cells occur at equinox (with similar magnitudes as in the Köln model), but with near-surface indirect cells over both poles. These shallow regions are the meridional manifestation of baroclinic eddies at the high latitudes (Lora and Mitchell, 2015).

3.2. Temperature

Zonal-mean temperatures at northern winter solstice from the IPSL model simulations are horizontally homogeneous at atmospheric pressures above 100 hPa, but have some latitudinal structure at lower pressures (Fig. 2a). Temperature minima, centered around 100 hPa, are symmetric about the equator (and coldest over the poles), but above that the highest temperatures occur at low latitudes, while the northern polar atmosphere between 10–30 hPa is much colder than its southern counterpart. At the northern vernal equinox, the temperature distribution is quite similar, except that both the

100 hPa southern polar region and the 10–30 hPa northern polar region have warmed by a few K (Fig. 2d). Thus, seasonal variations, though muted, are perceptible.

In the case of the Köln model, there is essentially no temperature variation with latitude at either season, meaning that temperature gradients are always minimal (Fig. 2b,e). This results directly from the tuning of the model to reproduce low-latitude observations. This approach has the side effect of strongly damping temperatures deviations elsewhere, and thus suppresses realistic temperature variations at other latitudes (and seasons).

The zonal-mean temperatures simulated by TAM show the largest (though still small) latitudinal variations near the surface, and similar solstitial variations as in the IPSL model above (Fig. 2c). In particular, equatorial temperatures are warmest, and the northern polar region sees the coldest temperatures. The differences are that the temperature minimum occurs at slightly higher pressures (around 130 hPa), and vertical temperature gradients above this level are somewhat stronger. The evolution of temperature into equinox is also quite similar, showing warming of both polar regions and little change at pressures above 300 hPa (Fig. 2f).

4. Low-latitude climatology and comparison to observations

We now focus specifically on the simulated climatology of the period following northern winter solstice, approximately corresponding to $L_S = 290$–$320°$, as this is the only time of year on Titan for which *in situ* data exist. This also permits predictions from the models for the same season in the future, which would coincide with the arrival of the proposed Dragonfly rotorcraft lander at Titan in 2034. In this subsection, the models' wind, temperature, and methane mole fraction fields are compared to those *in-situ* data from the Huygens probe, as a means of evaluating their fidelity, as well as in order to elucidate the inter-model spread.

4.1. Winds

Zonal winds simulated by the IPSL model are shown in Fig. 3a. Near the surface, these closely match the observed winds (Bird et al., 2005), with easterly winds of increasing magnitude with altitude below approximately 5 km. Above this level, the simulated winds become increasingly more westerly, as in the observed profile, but with insufficient shear; around 40 km altitude, the model winds are roughly 10 m s^{-1} slower than the observations. Nevertheless, these simulations qualitatively reproduce the observed wind structure. Meridional winds (Fig. 3b) are also in agreement with those inferred from the movement of the Huygens probe (Karkoschka, 2016), including near-surface northerlies and weak southerlies above that, with magnitudes close to zero aloft. The exception is the weak northward winds suggested at 15 km that exceed even the maximum winds at that level in the model.

The Köln model wind profiles are farthest from observations. The mean value of the zonal wind stays near zero at all altitudes in contrast to the substantial observed increase with altitude (Fig. 3e). The model's inability to reproduce Titan's zonal winds is apparent here, with the mismatch between simulations and measurements increasing with altitude. Near the surface, weak easterly zonal winds closely match observations. Meridional winds likewise match the inferred wind profile near the surface, though the simulations seem to produce several vertical layers of winds in opposing directions, rather than just the two observed and simulated by the other models. Above 5 km, the mean winds become increasingly northerly, instead of remaining at zero magnitude; in this case, however, the observed profile lies within the 1st–99th percentile range (see section 5.1) of the model (except around 15 km).

TAM wind fields agree best with the data (Fig. 3e, f), with the zonal wind profile proving an excellent match. There is a slight (1–3 m s^{-1}) overestimation of the zonal wind magnitude at most levels, but the wind direction and magnitudes closely reproduce the observed profile, including the higher vertical wind shear above 24 km than below. Additionally, the significant zonal wind increase with altitude accurately captures Titan's substantial equatorial superrotation. The model's meridional winds also generally match the observations albeit with weaker average magnitudes: in the boundary layer there is mean southerly flow underlain by mean northerly flow, as inferred from the movement of the Huygens probe. The average meridional wind profiles simulated by TAM and IPSL are practically identical, though the variability of the wind speed is considerably larger in the former. In this case, the nonzero northward winds inferred at 15 km fall well within the 1st–99th percentile envelope of the simulation.

4.2. Temperature and methane content

All three models simulate equatorial temperature profiles (Fig. 3c,g,k) that are in close agreement with that observed with the Huygens probe (Fulchignoni et al., 2005). The IPSL model simulates temperatures that are ∼1–2 K too cold between approximately 5 and 25 km altitudes, while TAM produces temperatures that are slightly (<1 K) too warm around 10 km altitude. The temperature structure from the Köln model is nearly identical to the observed profile below 30 km altitude, but it should be noted that this results from the fact that that model's radiative heating rates are tuned to reproduce the observations.

In all three models, temperatures near the temperature minimum (around 42 km) are slightly too warm. The same is true above these levels (not shown). Bézard et al. (2018) suggest that a similar discrepancy in results with a discrete ordinates one-dimensional model can be explained by adiabatic cooling due to rising motion; however, it is not clear whether the GCMs are all underestimating such a dynamical cooling, or whether these issues instead result from systematic inaccuracies or uncertainties in the radiative properties and/or profiles of atmospheric gases and haze.

The methane mole fraction profiles simulated by the models also qualitatively reproduce the measured profile (Niemann et al., 2010), though with several discrepancies. In all cases, the lowermost ∼5 km support constant mole fractions of methane, which indicate a well-mixed, subsaturated region, in agreement with the observation. Above this level, the mole fractions drop sharply and then asymptote to a minimum level around 40 km. This is strong evidence for methane being close to or at saturation between 5 and 40 km, though the compositions of liquid or solid droplets, and therefore the exact saturation values, are uncertain.

The IPSL model's profile has mole fractions that are generally slightly low (Fig. 3d), except at the surface. This is a result of the imposed rather than prognostic simulation of near-surface methane content, in combination with the model's colder-than-observed temperature profile. The Köln model and TAM both reproduce the observation remarkably well (considering, in particular, their simple treatment of saturation values), though in both cases the simulations slightly underestimate the observed methane mole fraction below around 10 km altitude. Near the surface, the observed profile lies within the 1st–99th percentile ranges of both models. In the Köln model, the methane content agrees very well with the observations above around 40 km altitude, despite the slightly warm temperatures. In TAM, the too-warm upper-level temperatures translate to methane mole fractions that are somewhat too large above roughly 30 km.

4.3. Latitudinal variations

Figure 4 shows zonal-mean latitudinal profiles of 10 m altitude wind fields (scaled from the models' lowest levels), as well as surface temperatures, for the early winter averaged over all simulated years for each model, over the low latitudes. The profiles show some structure and there is general qualitative agreement between models; there are also notable differences, but the range of variability in each model is larger than the differences of the displayed average profiles between models (see Sec. 5.2 for analysis of the variability).

The near-surface zonal winds (Fig. 4a) tend to shift from slightly westerly to slightly easterly between southern and northern low latitudes. The IPSL and Köln models indicate that the largest-magnitude average winds in the low latitudes occur between 20 and 30°S, while at that location TAM simulates near-zero average winds. Interestingly, the models coincide around 10°S, the latitude of the Huygens landing. They also agree in the northern hemisphere, where peak average easterlies occur in all cases between 10 and 25°N.

The simulated near-surface meridional winds (Fig. 4b) are northerly in all models, in agreement with the expectation of cross-equatorial return flow in the large-scale Hadley cell, with ascent in the southern hemisphere in this season. In all cases, the peak average winds occur close to the equator, but there is less agreement between the models regarding in which hemisphere. In addition, the Köln model and TAM suggest that mean southerlies exist poleward of around 25°S. In both of those cases, low-level convergence occurs throughout the southern low-latitudes, while in the IPSL model this occurs farther poleward.

Lastly, average surface temperature profiles (Fig. 4c) also coincide between models in predicting seasonal warmth in the low southern latitudes relative to the northern hemisphere. The IPSL model and TAM agree remarkably well in this range, though the maxima occur at different latitudes; this is likely a consequence of the differences in the treatment of surface methane and evaporation (see Sec. 6). The largest discrepancy is in the profile from the Köln model north of 15°N, which drops substantially and departs from the smoother profiles of the other two models; this behavior is likely also the result of localized liquid buildup that is evaporating (Tokano, 2019).

5. Variability

5.1. Variability in the atmospheric profiles

In addition to average values, Figure 3 displays the range of 1st–99th percentile, as well as absolute maximum and minimum values, in each simulation, calculated over all years for $L_S \approx 290$–$320°$. These statistics therefore give a sense of the range of diurnal to interannual variability for the season in question, as well as variability over longitude for IPSL and TAM (Köln results are averaged in longitude). While the temporal and spatial scales of variability are not individually resolved in this analysis, these statistics represent the full range of values simulated by the models.

Predictably, wind profiles are considerably more variable than temperature or methane mole fraction. This is because the thermal structure in Titan's lower atmosphere is largely controlled by radiative balance (McKay et al., 1989), and radiative timescales there are long (Bézard et al., 2018); at the same time, the methane mole fraction is strongly constrained by saturation, and therefore by the invariable temperature.

For zonal winds, both the IPSL model and TAM simulate 1st–99th percentile ranges of approximately 1–3 m s^{-1} around the mean values, in the former case increasing with altitude. The full range of simulated zonal winds is only slightly larger, though in TAM the range near the surface increases to between -5 and 5 m s^{-1}. This is likely a consequence of moist convection, which intermittently alters the boundary layer and affects the wind structure. For the Köln model, the range of variability is similar to IPSL near the surface, but increases with altitude and becomes increasingly asymmetric about the mean. Around 40 km altitude, the range of simulated winds is between around -0.5 and 5 m s^{-1}, while the mean value is approximately 1 m s^{-1}.

The relative variability of meridional winds shows more inter-model spread. IPSL simulates meridional winds that, above 5 km altitude, never exceed 0.5 m s^{-1} in magnitude. Closer to the surface, the range increases, with extrema reaching magnitudes of about 1 m s^{-1}. The spread of meridional winds in the Köln model is intermediate between the models, ranging from about ±0.5 m s^{-1} around the mean at roughly 5 km to ±1 m s^{-1} around the mean at 40 km and near the surface. The increase of the variability ranges with altitude above 5 km is also larger than for the other models, as with the case for zonal winds. Finally, TAM simulates meridional winds whose 1st–99th percentile range is approximately 1 m s^{-1} above and below the mean everywhere, with minima and maxima that exceed this by about another 0.5 m s^{-1}. Near the surface, these respective ranges roughly double.

The temperature variability in all cases is essentially negligible. This is in agreement with the fact that all observed low-latitude temperature profiles of Titan agree with each other remarkably well (Lindal et al., 1983; Fulchignoni et al., 2005; Schinder et al., 2011). In the Köln model and TAM, the range of temperatures around 40 km altitude is roughly 1 K around the mean (Fig. 3c,g). And, in TAM, extreme values deviate from the mean by up to several K near the surface, again likely as a result of relatively rare moist convective events, which the other models do not simulate.

Lastly, modest variability of the methane mole fraction appears in all of the models, with a few differences. As a result of its prescription at the surface, the variability in methane in the IPSL model is negligible at low altitudes, but the range increases with altitude to around 10 km, before decreasing again. Similar subtle mid-level ranges are produced in the other models, but in those cases the mole fraction below 5 km is most variable. In TAM, the 1st–99th percentile range is still fairly close to the mean, with more noticeable extrema, while in the Köln model the 1st–99th percentile range is relatively large from the surface to ∼5 km.

5.2. Surface and near-surface variability

Figure 5 displays the relative frequency distributions of surface and near-surface variables closest to 10°S, the latitude of the Huygens probe's landing, simulated by each model (for $L_S \approx 290$–$320°$). Each panel includes histograms of minimum, maximum, and daily-mean (averaged over one Tsol) values for each variable, illustrating the full range of variability for the season. The true frequency distribution of instantaneous values can be intuited from these histograms, but is not available given our data volume limitations.

Simulated wind speeds from the lowest model layers are scaled to 10 m winds for comparison. In all cases, these have magnitudes that rarely exceed 0.5 m s^{-1}, in agreement with observational estimates, though the distributions from the various models are quite different. Zonal winds average approximately zero, and both easterly and westerly winds occur in all models. Meridional winds average negative (that is, northerly) values, which agree with the inferred meridional wind from movement of the Huygens probe (Karkoschka, 2016).

The near-surface wind distributions from the IPSL model are weakly bimodal, with a secondary frequency maximum close to 0.5 m s^{-1} in zonal winds and close to zero in meridional winds (Fig. 5a,b). This is due to the influence of topography, which induces wind variations in longitude. The distributions of mean, maximum, and minimum winds are closely overlapping, so the range of diurnal-mean winds is representative of the full range. In the Köln model, the wind frequency distributions are narrower than in the other models (likely as a result of being zonal averages), and largely symmetric, with a somewhat larger relative spread between minimum and maximum than in the IPSL model (Fig. 5e,f). Lastly, the frequency distributions in TAM are more spread out than the other models, with extrema that extend relatively farther (Fig. 5i,j). These distributions are also not bimodal, since the model does not include topography. And the distributions of meridional winds are clearly positively skewed, though the highest frequencies of mean, minimum, and maximum are all still negative (northerly). In all models, the near-surface wind distributions agree very well with observational estimates.

Surface temperatures in the three models average between 93.5 and 94.0 K (Fig. 5c,g,k), in agreement with the value measured by Huygens (Fulchignoni et al., 2005). In the IPSL model, the frequency distributions have a secondary maximum just below 93.5 K, though the total range from minimum to maximum is limited to 93–94.5 K (Fig. 5c). The distributions from TAM are normal, and the range is similar with temperatures a few tenths of a degree higher (Fig. 5k). In the Köln model, the distribution of mean surface temperatures agrees with that of the other models, but does not overlap with the distributions of minimum and maximum temperatures (Fig. 5g). The minimum temperatures are around 93.0 K, while the maximum temperatures, which have a wider distribution, extend between 94.5–95.5 K, warmer than the other models. The reason for this model's considerably larger surface temperature variability is not obvious, though it is potentially related to the combination of topography and a low value of thermal inertia (IPSL uses a value of 1000 J m^{-2} $s^{-1/2}$ K^{-1}; Köln and TAM use a value of approximately 335 J m^{-2} $s^{-1/2}$ K^{-1}).

Substantial inter-model disagreement appears in the frequency distributions of boundary layer methane mole fraction (Fig. 5d,h,l). As discussed above, this iteration of the IPSL model prescribes the surface-level methane content, so its lack of variability and agreement with the observed value (Niemann et al., 2010) are expected and non-predictive. The other two models also agree well with the *in situ* measurement, which in both cases is the most frequent value. In both models the distributions of mean, minimum, and maximum mole fractions also largely overlap. On the other hand, the distributions are very different between models, with the Köln model simulating a much broader overall distribution (spanning 0.05–0.070) and TAM simulating a slightly positively skewed but very narrow distribution (spanning 0.055–0.060), with the exception of extremely infrequent maxima that also extend to 0.070. Whether these differences are attributable to the inclusion of a topography map in the former model, moist convection in the latter, or a deeper structural reason, is not clear.

Figure 6 shows the same relative frequency distributions of surface and near-surface fields as Fig. 5, but for latitudes close to 10°N, as a means of illustrating regional and seasonal variability across the low latitudes. In many regards, these distributions are similar to those at 10°S, but there are notable differences that are mainly attributable to the contrast between summer and winter hemispheres. Zonal winds in all models are more negative (more easterly), with the most common daily averages all falling below zero. Meridional winds remain generally negative, and in addition the westerly tails of the distributions are more negative, with no positive values simulated by the IPSL and Köln models; furthermore, the distributions in TAM are considerably less positively skewed.

The 10°N distributions of temperature are, in all models, slightly colder than in the south, again as a result of crossing from summer to winter hemispheres. In the IPSL model and TAM, the differences are slight, of less than 0.5 K (Fig. 6c,k); in the Köln model, the differences are of about 1 K, with the maximum value approximately 2 K colder (Fig. 6g). In addition, the latter model's surface temperature distributions overlap considerably more than in the south, with the range from minimum to maximum spanning approximately 92.5–94 K (as compared to 92.3–95.6 K in the south).

The distributions of methane mole fractions are least different across the equator. In the Köln model, the distributions extend to slightly lower values, with minima of around 0.048 (Fig. 6h); in TAM, the distribution is not skewed and the maximum values drop to approximately 0.060 (Fig 6l). (Again, the IPSL surface-level mole fractions are externally constrained, so no differences are expected or occur.)

5.3. Diurnal Variations

As a final intercomparison of the models' simulated variability, a subset of additional short (10 Tsol) simulations were run with sufficiently high output frequency to resolve diurnal variations. These were run for the time of year corresponding to $L_S \approx 305°$. Fig. 7 displays the resulting near-surface fields. In the IPSL and Köln models, the parameterized gravitational tide from Saturn induces a very regular diurnal variation in the surface pressure of around 0.05% and 0.1%, respectively (not shown; see Tokano and Neubauer, 2002); this effect is absent in TAM since the gravitational tide is not parameterized.

Both zonal and meridional 10 m winds in the IPSL model show almost no diurnal variations (Fig. 7a,d), though there is a hint of strengthening of northerly meridional winds in the local afternoon. Diurnal variations in near-surface winds exist in the Köln model, but in general their amplitude is considerably lower than day-to-day variability. Nevertheless, zonal winds appear to be slightly more westerly in the early morning and more easterly by early afternoon, while meridional winds appear more northerly in the morning than in the afternoon (Fig. 7b,e). In TAM, diurnal variations in winds are less perceptible, though there is a slight trend toward lower-magnitude winds, particularly in the zonal direction, during the afternoon (Fig. 7c). It should be noted that in all of these cases, 10 m winds are scaled from higher-altitude model levels, so subtle diurnal variations that would result from closer coupling to the surface may be missed.

Surface temperatures show the most appreciable diurnal variations (Fig. 7g,h,i). In the IPSL model, surface temperature changes are muted—consistent with the use of a relatively high surface thermal inertia—but nonetheless noticeable, peaking in the early afternoon. In the Köln model, surface temperature variability is particularly strong in the low-latitude southern hemisphere, in which some regions show up to 2 K changes between sunrise and afternoon highs. In the northern hemisphere, the diurnal contrasts are smaller due to the lower insolation, and the average day-to-night contrast is of about 1.5 K, with temperatures peaking around 15:00 local time. In TAM, a similar diurnal pattern appears but with much more muted magnitudes of roughly 0.3 K, despite the use of a relatively low surface thermal inertia. In all cases, the diurnal variations are discernible despite day-to-day and regional variability.

Lastly, the boundary layer methane mole fractions show no clear signature of diurnal variation. In the IPSL model, this results from the prescription of surface methane mole fraction. In the Köln model, individual grid points see substantial changes on short timescales, but there is no obvious diurnal pattern (Fig. 7d). In TAM, the methane mole fractions are nearly constant over the 10 Tsols analyzed (Fig. 7h). It should be noted that no precipitation occurred at these latitudes in the models during these short simulations.

6. Precipitation

The detection and monitoring of tropospheric clouds on Titan has been possible for about 20 years (Griffith et al., 2000; Brown et al., 2002; Roe et al., 2005; Porco et al., 2005; Schaller et al., 2006, 2009; Turtle et al., 2011a; Rodriguez et al., 2011; Roe, 2012; Turtle et al., 2018b) and the Cassini mission provided compelling evidence of copious precipitation events following large cloud outbursts (Turtle et al., 2011b). Cloud activity at mid- and high latitudes was common in the south during southern summer and early fall, and was observed to pick up in the north at the end of the Cassini mission, near the beginning of northern summer (Turtle et al., 2018b). In the most general terms, this seasonal evolution was predicted and expected (e.g., Mitchell et al., 2006), but the scarcity of low-latitude activity around the northern vernal equinox and dearth of clouds throughout northern spring was a puzzle in view of the idealized picture of a convergence and upwelling region traveling between the summer poles. Instead, consensus is emerging that restricted (polar) reservoirs of liquid methane—in the form of observed lakes and seas, but also of moist regolith and/or near-surface ground methane—are necessary to reproduce both the distribution and relatively sporadic occurrence of clouds (Mitchell and Lora, 2016; Lora and Ádámkovics, 2017; Faulk et al., 2017; Turtle et al., 2018b). Nevertheless, the details of Titan's hydrologic cycle are not yet fully understood, and represent a major open question post-Cassini.

While Cassini and ground-based instruments detected many polar and mid-latitude clouds around 2005, the environment measured *in situ* by Huygens at low latitudes was of a stable atmosphere with relatively low near-surface humidity (Fulchignoni et al., 2005; Niemann et al., 2010). These observations are in line with the expectation of relatively dry equatorial conditions that result from the long-term divergence of surface methane from the low-latitudes (Rannou et al., 2006; Mitchell, 2008). Thin stratiform layers of condensation were suggested based on the Huygens data (Tokano et al., 2006), but it is clear that moist convective events and significant precipitation would require a substantial perturbation from the measured profiles in order to initiate (Barth and Rafkin, 2007, 2010). Whether this is indication of seasonally dry conditions, or the result of a recent precipitation event stabilizing the atmosphere, is still under some debate.

Figure 8 shows the models' seasonal distributions of zonal-mean precipitation, averaged over the simulated years (see Table 1). The results from the IPSL model should be treated with some caution since the model's current configuration does not simulate a full methane cycle and includes prescribed surface methane mole fraction so that the atmospheric humidity is not freely simulated. The other two models do fully simulate the methane cycle, but with some substantial differences. First, TAM includes a parameterization of moist convection (Lora et al., 2015), while the Köln model does not (Tokano, 2019). Second, liquid methane produced by the large-scale condensation scheme is allowed to re-evaporate through the atmosphere as it falls in TAM, but is immediately precipitated to the surface in the Köln model. Perhaps most importantly, the surface boundary in both cases is a simple bucket scheme, but with very different assumptions: In TAM, the polar regions have effectively inexhaustible surface methane and a modest infiltration rate is implemented at low latitudes (Lora and Mitchell, 2015; Lora and Ádámkovics, 2017; Faulk et al., 2017), and any surface methane is fully available to the atmosphere. In contrast, the Köln model is initialized with a dry surface, there is no infiltration, and evaporation rates are scaled with an arbitrary "availability factor" of 0.5 (Tokano, 2019). In addition, the Köln model includes the topography map of Lorenz et al. (2013). The resulting precipitation distributions, while similar in the most general terms, are quite different in detail [compare Fig. 1 of Faulk et al. (2017) to Fig. 13 of Tokano (2019)].

The precipitation distribution from the IPSL model simulation follows seasonal patterns, with peak precipitation rates occurring during summertime over both poles, and mild precipitation occurring at low and mid-latitudes primarily in spring and summer (Fig. 8a). But precipitation tends to occur quasi-continuously in many regions, which is inconsistent with Cassini observations (e.g., Turtle et al., 2018b). In addition, there appear to be latitudes of preferred precipitation, likely as a result of the numerical noise also observed in the meridional streamfunction (Fig. 1d) and associated with the implementation of topography.

Precipitation in the other models is more sporadic (Fig. 8b,c). In both cases the most precipitation also falls over the polar regions, but occurs roughly from mid-spring to mid-summer (that is, earlier in the season than in the IPSL model). This is probably due to differences in the thermal inertia of the surface used by the models. At lower latitudes, more precipitation falls in the northern than the southern hemisphere in both models, though in the Köln model simulation northern mid-latitude precipitation falls generally year-round, while southern mid-latitude precipitation is almost negligible and equatorial precipitation mostly occurs around northern summer solstice, contradicting observations of clouds. In TAM, the seasonality is more obvious and precipitation generally occurs in summer mid-latitudes and equinoctial low-latitudes. It is worth noting that—assuming precipitation is a good proxy for clouds—this model's overall precipitation distribution compares favorably with the distribution of observed clouds (Mitchell and Lora, 2016; Faulk et al., 2017; Turtle et al., 2018b), and also exhibits intensity statistics that correlate with the latitude distribution of alluvial fans (Faulk et al., 2017).

Figure 9 shows time series of precipitation over the low latitudes averaged over the simulated years (see Table 1). In the IPSL model, precipitation is generally higher in the southern low latitudes than the northern, and precipitation rates in both hemispheres increase, from a minimum just after summer solstice, into the subsequent season. This means that the season of interest, shortly after southern summer solstice ($L_S = 290$–$320°$), sees near-minimum levels of precipitation, which in the northern low latitudes in particular are almost zero. In the southern low latitudes, the indicated persistent all-year precipitation is incompatible with the presence of sand dunes throughout the region, which require that the sand be at least sometimes dry. A robust interpretation of the dunes would require a better sense of the character of rainfall and subsequent drying, which is not treated in this model.

Low-latitude precipitation time series from the Köln model are shown in the second row of Fig. 9. Average precipitation rates are always low (<2.5 mm Tsol^{-1}), and precipitation is quite continuous, which would imply more continuous cloud coverage than observed. The maximum in both northern and southern low latitudes occurs around northern summer solstice, and this is followed by very low precipitation rates through winter solstice, and then a slight increase during northern winter. The relative symmetry between hemispheres at these low latitudes appears to result from the effects of topography in this model, since the overall distribution of precipitation is more asymmetric in simulations without it (Tokano, 2019). The model predicts a high frequency of at least weak near-equatorial precipitation between $L_S = 290$ and 320°; however, only a handful of low-latitude cloud events (∼5) were observed by Cassini during this period (Turtle et al., 2018b), contradicting the simulations.

Low-latitude precipitation in TAM (Fig. 9, third row) behaves quite differently. The results are averages over 20 simulated years so precipitation appears more common than any individual year actually is, but nevertheless there is clear indication of intermittency. In addition, the (mean) precipitation rates extend up to 8.0 mm Tsol^{-1}, indicating that some precipitation events are intense (Faulk et al., 2017), in these regions particularly around northern summer solstice ($L_S \sim 90°$). Lastly, precipitation is almost entirely absent during northern winter, and in particular does not occur at all during $L_S = 290$–$320°$. (Indeed, in the 50 years of simulation used in Faulk et al. (2017), no precipitation ever occurred at these low latitudes in this range of L_S.) Its prediction of extended droughts with highly episodic rainfall is also consistent with the existence of sand dunes. Therefore, TAM appears to capture many aspects of observed Titan meteorology and its manifestations in the landscape. Lastly, the presence of methane moisture at the Huygens landing site (Lorenz et al., 2006a; Karkoschka and Tomasko, 2009; Niemann et al., 2010) is compatible with the last rainfall having occurred there some time before, as suggested in Fig. 9; the landing site was a stream bed, and since ethane was also present, evaporation of methane may have been substantially depressed, therefore allowing near-surface methane to persist long after precipitation.

7. Discussion and Conclusions

We have presented a comparison of three GCMs of Titan's atmosphere to each other and to *in situ* data. This generation of models, at the end of the Cassini mission's exploration of the Saturn system, contains numerous improvements and modifications that have increased the realism and fidelity of the simulations. In many respects the models agree well with the observations (and each other), though there remain a number of discrepancies, as well as various aspects that make the models somewhat incommensurable.

It is nevertheless clear that the *in situ* measurements taken by the Huygens probe are generally representative of Titan's low-latitude atmosphere, as also borne out by comparison to other observations (Lindal et al., 1983; Schinder et al., 2011), and the three GCMs studied here do a reasonable job of reproducing the observed low-latitude environment. The possible exception to this is the simulation of zonal winds above 5 km altitudes, which only one of the models (TAM) reproduces in a quantitatively satisfactory way. Furthermore, it is also apparent that, despite differences in the simulated variability, the average expected values for low-level winds, surface temperatures, and, to a lesser extent, boundary layer humidities during northern winter are fairly well constrained. Even the magnitudes of plausible variability in the models are qualitatively similar.

Other specific findings, as well as some predictions for the low-latitude environment during northern winter, have resulted from these comparisons:

- Titan's strong zonal winds and concomitant superrotation remain challenging for models to reproduce precisely, but two models clearly attain superrotating winds and one accurately reproduces the Huygens wind profile
- The variability of zonal winds is small in all models, with 1st–99th percentile values generally less than 5 m s^{-1} from the climatological means for the lower atmosphere
- 10 m altitude winds rarely exceed magnitudes of 0.5 m s^{-1}
- 10 m altitude meridional winds generally blow from the north, in agreement with expectations from large-scale circulation arguments
- Meridional winds are weak in models and observations in the boundary layer, and nearly zero above, with 1st–99th percentile values less than $\sim$1 m s^{-1} from the climatological mean (though inter-model variability is large in this regard)

- Atmospheric temperatures are highly invariable, in agreement with various prior observations

- Surface temperature variations are small but noticeable (in agreement with Cottini et al., 2012), and are also the clearest indication of diurnal variation, which shows substantial inter-model spread

The largest differences between the models concern the methane cycle, though we emphasize that this is also the area in which structural differences make intercomparison least meaningful. As has been shown in a range of contexts, the amount and distribution of surface methane, and its availability to the atmosphere, strongly affects the atmospheric humidity, moisture transport, and precipitation frequency and distribution (Mitchell et al., 2006; Mitchell, 2008; Mitchell et al., 2009; Tokano, 2009; Schneider et al., 2012; Lora et al., 2015; Lora and Mitchell, 2015; Mitchell and Lora, 2016; Newman et al., 2016; Lora and Ádámkovics, 2017; Faulk et al., 2017; Turtle et al., 2018b), yet this remains one of the least constrained variables in Titan's hydrologic cycle. But this presents a considerable opportunity for future data—both in the form of continued remote monitoring of cloud activity and with future *in situ* measurements by the proposed Dragonfly mission concept—to make high-impact contributions to our understanding of Titan and its climate system.

This study offers further suggestion that future measurements of Titan's lower atmosphere and surface environments, at low latitudes, will on average not be very different from measurements made by Voyager, Cassini, and Huygens. But the ability to characterize the range of variability of various fields, as well as its timescales, will provide invaluable input to further differentiating between successful and unsuccessful model configurations and assumptions, and thereby improve our ability to assess underlying physical mechanisms. In addition, future data that provides improved information on regional variations will significantly enhance our understanding of the processes affecting the connection between Titan's surface and atmosphere. Refining our process understanding through improved data and more detailed interpretation with models will also inform characterization efforts of Titan's broader global climate, including the relationship between high and low latitudes, the global methane cycle, and seasonal changes therein.

Acknowledgements

TT is funded by the Deutsche Forschungsgemeinschaft (DFG, German Research Foundation) Grant TO269/4-2. The IPSL simulations were run on High-Performance Computing (HPC) resources of Centre Informatique National de l'Enseignement Supérieur (CINES), allocations n°A0020101167 and A0040110391 made by Grand Équipement National de Calcul Intensif (GENCI).

References

Barth, E. K., Rafkin, C. R., 2007. TRAMS: A new dynamic cloud model for Titan's methane clouds. Geophys. Res. Lett. 34, L03203.

Barth, E. L., Rafkin, S. C. R., 2010. Convective cloud heights as a diagnostic for methane environment on Titan. Icarus 206, 467–484.

Bézard, B., Vinatier, S., Achterberg, R. K., 2018. Seasonal radiative modeling of Titan's stratospheric temperatures at low latitudes. Icarus 302, 437–450.

Bird, M. K., Allison, M., Asmar, S. W., Atkinson, D. H., Avruch, I. M., Dutta-Roy, R., Dzierma, Y., Edenhofer, P., Folkner, W. M., Gurvits, L. I., Johnston, D. V., Plettemeier, D., Pogrebenko, S. V., Preston, R. A., Tyler, G. L., 2005. The vertical profile of winds on Titan. Nature 438, 800–802.

Brown, M. E., Bouchez, A. H., Griffith, C. A., 2002. Direct detection of variable tropospheric clouds near Titan's south pole. Nature 420, 795–797.

Cottini, V., Nixon, C. A., Jennings, D. E., de Kok, R., Teanby, N. A., Irwin, P. G. J., Flasar, F. M., 2012. Spatial and temporal variations in Titan's surface temperatures from Cassini CIRS observations. Planet. Space Sci. 60, 62–71.

Crespin, A., Lebonnois, S., Vinatier, S., Bézard, B., Coustenis, A., Teanby, N. A., Achterberg, R. K., Rannou, P., Hourdin, F., 2008. Diagnostics of Titan's stratospheric dynamics using Cassini/CIRS data and the 2-dimensional IPSL circulation model. Icarus 197, 556–571.

Eyring, V., Bony, S., Meehl, G. A., Senior, C. A., Stevens, B., Stouffer, R. J., Taylor, K. E., 2016. Overview of the Coupled Model Intercomparison Project phase 6 (CMIP6) experimental design and organization. Geosci. Model Dev. 9, 1937–1958.

Faulk, S. P., Moon, S., Mitchell, J. L., Lora, J. M., 2017. Regional patterns of extreme precipitation on Titan consistent with observed alluvial fan distribution. Nature Geosci. 10, 827–831.

Fulchignoni, M., Ferri, F., Angrilli, F., Ball, A. J., Bar-Nun, A., Barucci, M. A., Bettanini, C., Bianchini, G., Borucki, W., Colombatti, G., Coradini, M., Coustenis, A., Debei, S., Falkner, P., Fanti, G., Flamini, E., Gaborit, V., Grard, R., Hamelin, M., Harri, A. M., Hathi, B., Jernej, I., Leese, M. R., Lehto, A., Lion Stoppato, P. F., López-Moreno, J. J., Mäkinen, T., McDonnell, J. A. M., McKay, C. P., Molina-Cuberos, G., Neubauer, F. M., Pirronello, V., Rodrigo, R., Saggin, B., Schwingenschuh, K., Seiff, A., Simões, F., Svedhem, H., Tokano, T., Towner, M. C., Trautner, R., Withers, P., Zarnecki, J. C., 2005. In situ measurements of the physical characteristics of Titan's environment. Nature 438, 785–791.

Griffith, C. A., Hall, J. L., Geballe, T. R., 2000. Detection of daily clouds on Titan. Science 290, 509–513.

Griffith, C. A., Rafkin, S., Rannou, P., McKay, C. P., 2014. Storms, clouds, and weather. In: Müller-Wodarg, I., Griffith, C. A., Lellouch, E., Cravens, T. E. (Eds.), Titan: Interior, surface, atmosphere, and space environment. Cambridge University Press, Cambridge, pp. 190–223.

Hayes, A., Aharonson, O., Callahan, P., Elachi, C., Gim, Y., Kirk, R., Lewis, K., Lopes, R., Lorenz, R., Lunine, J., Mitchell, K., Mitri, G., Stofan, E., Wall, S., 2008. Hydrocarbon lakes on Titan: Distribution and interaction with a porous regolith. Geophys. Res. Lett. 35, L09204.

Hayes, A., Lorenz, R., Donelan, M., Manga, M., Lunine, J., Schneider, T., Lamb, M., Mitchell, J., Fischer, W., Graves, S., Tolman, H., Aharonson, O., Encrenaz, P., Ventura, B., Casarano, D., Notarnicola, C., 2013. Wind driven capillary-gravity waves on Titan's lakes: Hard to detect or non-existent? Icarus 225, 403–412.

Hayes, A. G., 2016. The lakes and seas of Titan. Ann. Rev. Earth Planet. Sci. 44, 57–83.

Karkoschka, E., 2007. DISR imaging and the geometry of the descent of the Huygens probe within Titan's atmosphere. Planet. Space Sci. 55, 1896–1935.

Karkoschka, E., 2016. Titan's meridional wind profile and Huygens' orientation and swing inferred from the geometry of DISR imaging. Icarus 270, 326–338.

Karkoschka, E., Tomasko, M. G., 2009. Rain and dewdrops on Titan based on in situ imaging. Icarus 199, 442–448.

Lavvas, P., Yelle, R., Griffith, C., 2010. Titan's vertical aerosol structure at the Huygens landing site: Constraints on particle size, density, and refractive index. Icarus 210, 832–842.

Lebonnois, S., Burgalat, J., Rannou, P., Charnay, B., 2012. Titan global climate model: A new 3-dimensional version of the IPSL Titan GCM. Icarus 218, 707–722.

Lebonnois, S., Lee, C., Yamamoto, M., Dawson, J., Lewis, S. R., Mendonca, J., Read, P. L., Parish, H. F., Schubert, G., Bengtsson, L., Grinspoon, D., Limaye, S. S., Schmidt, H., Svedhem, H., Titov, D. V., 2013. Models of venus atmosphere. In: Towards understanding the climate of Venus. ISSI Scientific Report Series, vol 11. Springer, New York, pp. 129–156.

Lindal, G. F., Wood, G. E., Hotz, H. B., Sweetnam, D. N., Eshleman, V. R., Tyler, G. L., 1983. The atmosphere of Titan — an analysis of the Voyager 1 radio occultation measurements. Icarus 53, 348–363.

Lora, J. M., Ádámkovics, M., 2017. The near-surface methane humidity on Titan. Icarus 286, 270–279.

Lora, J. M., Lunine, J. I., Russell, J. L., 2015. GCM simulations of Titan's middle and lower atmosphere and comparison to observations. Icarus 250, 516–528.

Lora, J. M., Mitchell, J. L., 2015. Titan's asymmetric lake distribution mediated by methane transport due to atmospheric eddies. Geophys. Res. Lett. 42, 6213–6220.

Lorenz, R. D., 2006. Thermal interactions of the Huygens probe with the Titan environment: constraint on near-surface wind. Icarus 182, 559–566.

Lorenz, R. D., Newman, C. E., Tokano, T., Mitchell, J. L., Charnay, B., Lebonnois, S., Achterberg, R. K., 2012. Formulation of a wind specification for Titan late polar summer exploration. Planet. Space Sci. 70, 73–83.

Lorenz, R. D., Niemann, H., Harpold, D., Zarnecki, J., 2006a. Titan's damp ground: constraints on Titan surface thermal properties from the temperature evolution of the Huygens GCMS inlet. Meteoritics and Planetary Science 41, 1405–1414.

Lorenz, R. D., Stiles, B. W., Aharonson, O., Lucas, A., Hayes, A. G., Kirk, R. L., Zebker, H. A., Turtle, E. P., Neish, C. D., Stofan, E. R., Barnes,

J. W., the Cassini RADAR team, 2013. A global topographic map of Titan. Icarus 225, 367–377.

Lorenz, R. D., Turtle, E. P., Barnes, J. W., Trainer, M. G., Adams, D. S., Hibbard, K. E., Sheldon, C. Z., Zacny, K., Peplowski, P. N., Lawrence, D. J., Ravine, M. A., McGee, T. G., Sotzen, K. S., MacKenzie, S. M., Langelaan, J. W., Schmitz, S., Wolfarth, L. S., Bedini, P. D., 2018. Dragonfly: A rotorcraft lander concept for scientific exploration at Titan. Johns Hopkins APL Technical Digest 34, 374–387.

Lorenz, R. D., Wall, S., Radebaugh, J., Boubin, G., Reffet, E., Janssen, M., Stofan, E., Lopes, R., Kirk, R., Elachi, C., Lunine, J., Mitchell, K., Paganelli, F., Soderblom, L., Wood, C., Wye, L., Zebker, H., Anderson, Y., Ostro, S., Allison, M., Boehmer, R., Callahan, P., Encrenaz, P., Ori, G. G., Francescetti, G., Gim, Y., Hamilton, G., Hensley, S., Johnson, W., Kelleher, K., Muhleman, D., Picardi, G., Posa, F., Roth, L., Seu, R., Shaffer, S., Stiles, B., Vetrella, S., Flamini, E., West, R., 2006b. The sand seas of Titan: Cassini RADAR observations of longitudinal dunes. Science 312, 724–727.

McDonald, G. D., Hayes, A. G., Ewing, R. C., Lora, J. M., Newman, C. E., Tokano, T., Lucas, A., Soto, A., Chen, G., 2016. Variations in Titan's dune orientations as a result of orbital forcing. Icarus 270, 197–210.

McKay, C. P., Pollack, J. B., Courtin, R., 1989. The thermal structure of Titan's atmosphere. Icarus 80, 23–53.

Mitchell, J. L., 2008. The drying of Titan's dunes: Titan's methane hydrology and its impact on atmospheric circulation. J. Geophys. Res. 113, E08015.

Mitchell, J. L., Ádámkovics, M., Caballero, R., Turtle, E. P., 2011. Locally enhanced precipitation organized by planetary-scale waves on Titan. Nature Geosci. 4, 589–592.

Mitchell, J. L., Lora, J. M., 2016. The climate of Titan. Ann. Rev. Earth Planet. Sci. 44, 353–380.

Mitchell, J. L., Pierrehumbert, R. T., Frierson, D. M. W., Caballero, R., 2006. The dynamics behind Titan's methane clouds. Proc. Natl. Acad. Sci. 103, 18421–18426.

Mitchell, J. L., Pierrehumbert, R. T., Frierson, D. M. W., Caballero, R., 2009. The impact of methane thermodynamics on seasonal convection and circulation in a model Titan atmosphere. Icarus 203, 250–264.

Newman, C. E., Richardson, M. I., Lian, Y., Lee, C., 2016. Simulating Titan's methane cycle with the TitanWRF general circulation model. Icarus 267, 106–134.

Niemann, H. B., Atreya, S. K., Bauer, S. J., Carignan, G. R., Demick, J. E., Frost, R. L., Gautier, D., Haberman, J. A., Harpold, D. N., Hunten, D. M., Israel, G., Lunine, J. I., Kasprzak, W. T., Owen, T. C., Paulkovich, M., Raulin, F., Raaen, E., Way, S. H., Dec. 2005. The abundances of constituents of Titan's atmosphere from the GCMS instrument on the Huygens probe. Nature 438, 779–784.

Niemann, H. B., Atreya, S. K., Demick, J. E., Gautier, D., Haberman, J. A., Harpold, D. N., Kasprzak, W. T., Lunine, J. I., Owen, T. C., Raulin, F., 2010. Composition of Titan's lower atmosphere and simple surface volatiles as measured by the Cassini-Huygens probe gas chromatograph mass spectrometer experiment. J. Geophys. Res. 115, E12006.

Poggiali, V., Mastrogiuseppe, M., Hayes, A. G., Seu, R., Birch, S. P. D., Lorenz, R., Grima, C., Hofgartner, J. D., 2016. Liquid-filled canyons on Titan. Geophys. Res. Lett. 43, 7887–7894.

Porco, C., Baker, E., Barbara, J., Beurle, K., Brahic, A., Burns, J. A., Charnoz, S., Cooper, N., Dawson, D., Del Genio, A., Denk, T., Dones, L., Dyudina, U., Evans, M., Fussner, S., Giese, B., Grazier, K., Helfenstein, P., Ingersoll, A., Jacobson, R. A., Johnson, T., McEwen, A., Murray, C., Neukum, G., Owen, W., Perry, J., Roatsch, T., Spitale, J., Squyres, S., Thomas, P., Tiscareno, M., Turtle, E., Vasavada, A., Veverka, J., Wagner, R., West, R., 2005. Imaging of Titan from the Cassini spacecraft. Nature 434, 159–168.

Radebaugh, J., Lorenz, R. D., Lunine, J. I., Wall, S. D., Boubin, G., Reffet, E., Kirk, R. L., Lopes, R. M., Stofan, E. R., Soderblom, L., Allison, M., Janssen, M., Paillou, P., Callahan, P., Spencer, C., The Cassini Radar Team, 2008. Dunes on Titan observed by Cassini Radar. Icarus 194, 690–703.

Rannou, P., Montmessin, F., Hourdin, F., Lebonnois, S., 2006. The latitudinal distribution of clouds on Titan. Science 311, 201–205.

Rodriguez, S., Le Mouelic, S., Rannou, P., Sotin, C., Brown, R. H., Barnes, J. W., Griffith, C. A., Burgalat, J., Baines, K. H., Buratti, B. J., Clark, R. N., Nicholson, P. D., 2011. Titan's cloud seasonal activity from winter to spring with Cassini/VIMS. Icarus 216, 89–110.

Roe, H. G., 2012. Titan's methane weather. Ann. Rev. Earth Planet. Sci. 40, 355–382.

Roe, H. G., Bouchez, A. H., Trujillo, C. A., Schaller, E. L., Brown, M. E., 2005. Discovery of temperate latitude clouds on Titan. Astrophys. J. 618, L49–L52.

Schaller, E. L., Brown, M. E., Roe, H. G., Bouchez, A. H., 2006. A large cloud outburst at Titan's south pole. Icarus 182, 224–229.

Schaller, E. L., Roe, H. G., Schneider, T., Brown, M. E., 2009. Storms in the tropics of Titan. Nature 460, 873–875.

Schinder, P. J., Flasar, F. M., Marouf, E. A., French, R. G., McGhee, C. A., Kliore, A. J., Rappaport, N. J., Barbinis, E., Fleischman, D., Anabtawi, A., 2011. The structure of Titan's atmosphere from Cassini radio occultations. Icarus 215, 460–474.

Schneider, T., Graves, S. D. B., Schaller, E. L., Brown, M. E., 2012. Polar methane accumulation and rainstorms on Titan from simulations of the methane cycle. Nature 481, 58–61.

Schröder, S., Karkoschka, E., Lorenz, R., 2012. Bouncing on Titan: Motion of the Huygens probe in the seconds after landing. Planet. Space Sci. 73, 327–340.

Stofan, E. R., Elachi, C., Lunine, J. I., Lorenz, R. D., Stiles, B., Mitchell, K. L., Ostro, S., Soderblom, L., Wood, C., Zebker, H., Wall, S., Janssen, M., Kirk, R., Lopes, R., Paganelli, F., Radebaugh, J., Wye, L., Anderson, Y., Allison, M., Boehmer, R., Callahan, P., Encrenaz, P., Flamini, E., Francescetti, G., Gim, Y., Hamilton, G., Hensley, S., Johnson, W. T. K., Kelleher, K., Muhleman, D., Paillou, P., Picardi, G., Posa, F., Roth, L., Seu, R., Shaffer, S., Vetrella, S., West, R., Jan. 2007. The lakes of Titan. Nature 445, 61–64.

Tokano, T., 2009. Impact of seas/lakes on polar meteorology of Titan: Simulation by a coupled GCM-Sea model. Icarus 204, 619–636.

Tokano, T., 2013. Wind-induced equatorial bulge in Venus and Titan general circulation models: Implications for the simulation of superrotation. Geophys. Res. Lett. 40, 4538–4543.

Tokano, T., 2019. Orbitally and geographically caused seasonal asymmetry in Titan's tropospheric climate and its implications for the lake distribution. Icarus 317, 337–353.

Tokano, T., McKay, C. P., Neubauer, F. M., Atreya, S. K., Ferri, F., Fulchignoni, M., Niemann, H. B., 2006. Methane drizzle on Titan. Nature 442, 432–435.

Tokano, T., Neubauer, F. M., 2002. Tidal winds on Titan caused by Saturn. Icarus 158, 499–515.

Tokano, T., Neubauer, F. M., Laube, M., McKay, C. P., 1999. Seasonal variation of Titan's atmospheric structure simulated by a general circulation model. Planet. Space Sci. 47, 493–520.

Tomasko, M., Bézard, B., Doose, L., Engel, S., Karkoschka, E., 2008a. Measurements of methane absorption by the descent imager/spectral radiometer (DISR) during its descent through Titan's atmosphere. Planet. Space Sci. 56 (5), 624–647.

Tomasko, M., Doose, L., Engel, S., Dafoe, L., West, R., Lemmon, M., Karkoschka, E., See, C., 2008b. A model of Titan's aerosols based on measurements made inside the atmosphere. Planet. Space Sci. 56 (5), 669–707.

Tomasko, M. G., Archinal, B., Becker, T., Bézard, B., Bushroe, M., Combes, M., Cook, D., Coustenis, A., de Bergh, C., Dafoe, L. E., Doose, L., Douté, S., Eibl, A., Engel, S., Gliem, F., Grieger, B., Holso, K., Howington-Kraus, E., Karkoschka, E., Keller, H. U., Kirk, R., Kramm, R., Küppers, M., Lanagan, P., Lellouch, E., Lemmon, M., Lunine, J., McFarlane, E., Moores, J., Prout, G. M., Rizk, B., Rosiek, M., Rueffer, P., Schröder, S. E., Schmitt, B., See, C., Smith, P., Soderblom, L., Thomas, N., West, R., 2005. Rain, winds and haze during the Huygens probe's descent to Titan's surface. Nature 438, 765–778.

Tomasko, M. G., Bézard, B., Doose, L., Engel, S., Karkoschka, E., Vinatier, S., 2008c. Heat balance in Titan's atmosphere. Planet. Space Sci. 56, 648–659.

Turtle, E. P., Barnes, J. W., Trainer, M. G., Lorenz, R. D., Hibbard, K. E., Adams, D. S., Bedini, P., Brinckerhoff, W. B., Cable, M. L., Ernst, C., Freissinet, C., Hand, K., Hayes, A. G., Horst, S. M., Johnson, J. R., Karkoschka, E., Langelaan, J. W., Lawrence, D. J., Le Gall, A., Lora, J. M., MacKenzie, S. M., McKay, C. P., Neish, C. D., Newman, C. E., Palacios, J., Panning, M. P., Parsons, A. M., Peplowski, P. N., Radebaugh, J., Rafkin, S. C. R., Ravine, M. A., Schmitz, S., Soderblom, J. M., Sotzen, K. S., Stickle, A. M., Stofan, E. R., Tokano, T., Wilson, C., Yingst, R. A., Zacny, K., March 2018a. Dragonfly: In situ exploration of Titan's organic chemistry and habitability. In: 49th Lunar and Planetary Science Conference. Houston, TX. Abstract #1641.

Turtle, E. P., Del Genio, A. D., Barbara, J. M., Perry, J. E., Schaller, E. L., McEwen, A. S., West, R. A., Ray, T. L., 2011a. Seasonal changes in Titan's meteorology. Geophys. Res. Lett. 38, L03203.

Turtle, E. P., Perry, J. E., Barbara, J. M., Del Genio, A. D., Rodriguez, S., Sotin, C., Lora, J. M., Faulk, S., Corlies, P., Kelland, J., MacKenzie, S. M., West, R. A., McEwen, A. S., Lunine, J. I., Pitesky, J., Ray, T. L., Roy, M., 2018b. Titan's meteorology over the Cassini mission: Evidence for extensive subsurface methane reservoirs. Geophys. Res. Lett. 45, 5320–5328.

Turtle, E. P., Perry, J. E., Hayes, A. G., Lorenz, R. D., Barnes, J. W., McEwen, A. S., West, R. A., Del Genio, A. D., Barbara, J. M., Lunine, J. I., Schaller, E. L., Ray, T. L., Lopes, R. M. C., Stofan, E. R., 2011b. Rapid and extensive surface changes near Titan's equator: Evidence of April showers. Science 331, 1414–1417.

Turtle, E. P., Perry, J. E., Hayes, A. G., McEwen, A. S., 2011c. Shoreline retreat at Titan's Ontario Lacus and Arrakis Planitia from Cassini Imaging Science Subsystem observations. Icarus 212, 957–959.

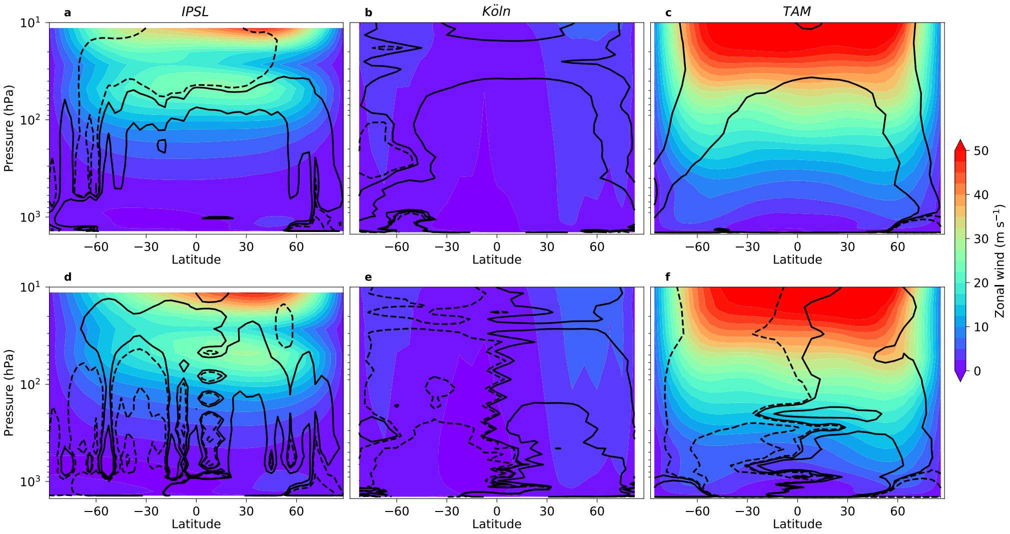

Figure 1: Zonal-mean zonal winds (colors) and meridional mass streamfunction (contours) for northern winter solstice (top row) and northern vernal equinox (bottom row). The columns show the results for different models. Positive zonal winds indicate westerlies (eastward). The contours show values of the streamfunction of ± 0.1 and 0.01×10^9 kg s^{-1}; solid (positive) contours indicate clockwise motion and dashed (negative) contours indicate counterclockwise motion.

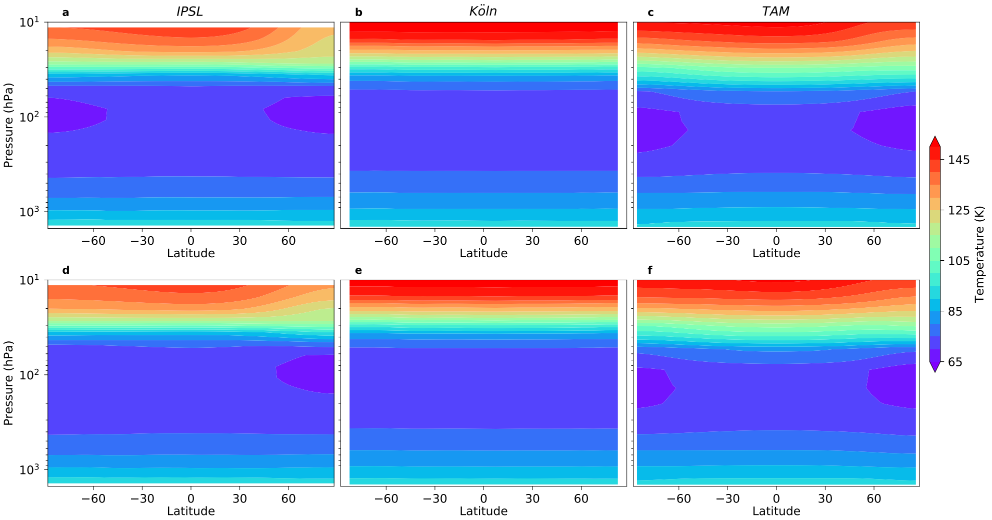

Figure 2: Zonal-mean air temperatures for northern winter solstice (top row) and northern vernal equinox (bottom row). The columns show the results for different models.

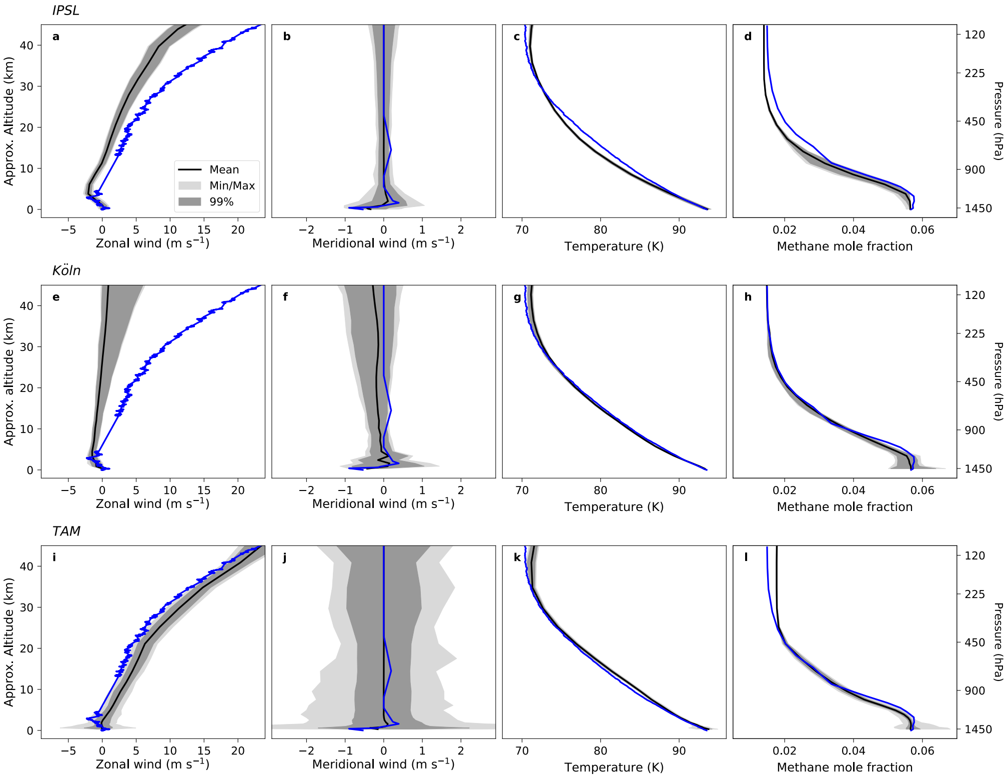

Figure 3: Vertical profiles of (columns from left to right) zonal winds, meridional winds, temperatures, and methane mole fractions simulated by the models and as measured *in situ* (blue curves) (Bird et al., 2005; Karkoschka, 2016; Fulchignoni et al., 2005; Niemann et al., 2010). Model results are shown at the grid point latitude closest to the Huygens probe landing at 10°S, considering all longitudes. Shaded regions show the ranges of minimum to maximum values (light gray) and 1st to 99th percentiles (dark gray), with the mean values for the season shown as black curves. The various rows show the results for different models. Positive zonal winds indicate westerlies (eastward), while positive meridional winds indicate southerlies (northward).

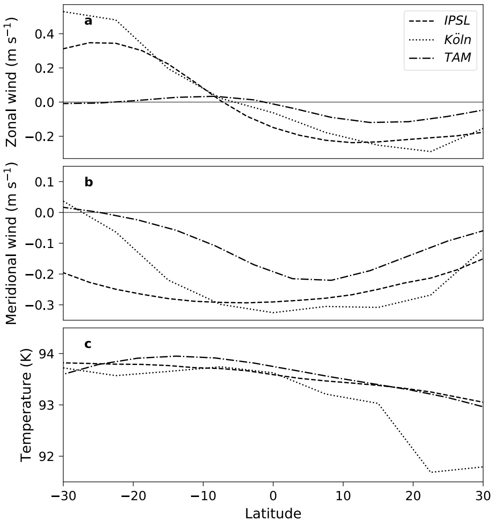

Figure 4: Latitudinal profiles of zonal-mean near-surface winds and surface temperatures, averaged between $L_S \approx 290$–$320°$ and over all simulated years (see Table 1).

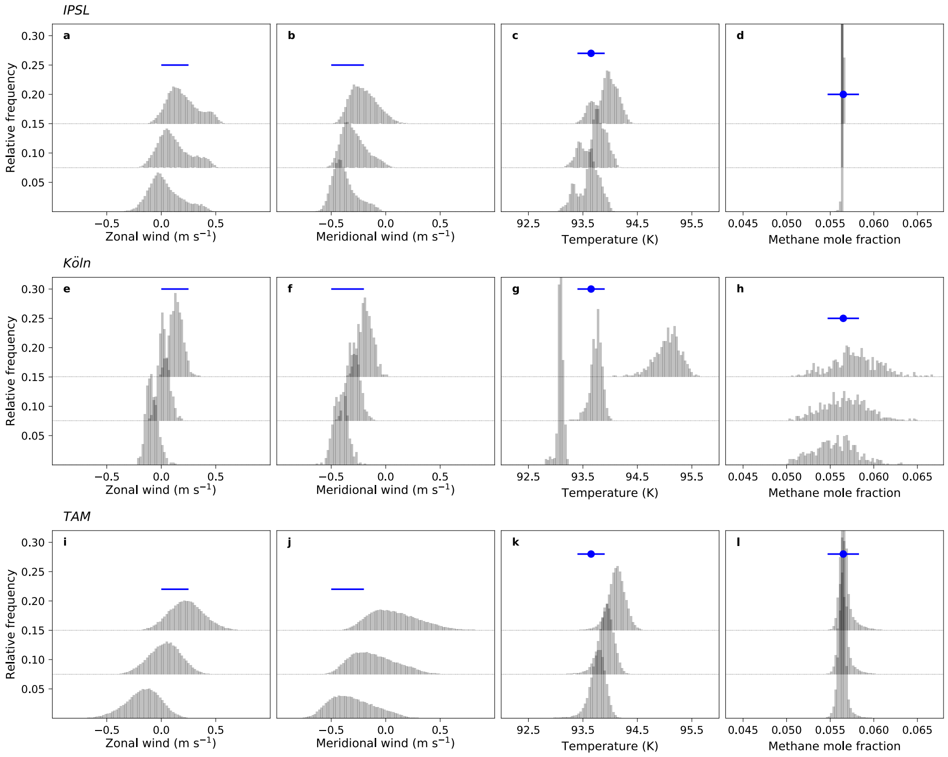

Figure 5: Histograms of (columns from left to right) near-surface winds, surface temperatures, and boundary layer methane mole fraction. Results are shown for model grid points closest to the Huygens probe landing at 10°S, considering all longitudes (results for the Köln model are zonal averages). Histograms for daily minimum, mean, and maximum values are shown in each panel—offset vertically from 0 to 0.15—to fully illustrate the range of variability in each simulation. For winds (left two columns), bottom-layer model results were scaled to 10 m above the surface. Methane mole fractions (right column) are shown for the bottom model layers, which are approximately at 40 m for the IPSL model, and 300 m for both the Köln model and TAM. In each panel, blue markers indicate observational estimates of winds (Lorenz, 2006; Karkoschka, 2007; Schröder et al., 2012) or measurements, with reported uncertainties, of temperature (Fulchignoni et al., 2005) and methane mole fraction (Niemann et al., 2010). The vertical position of these markers is arbitrary and chosen for clarity.

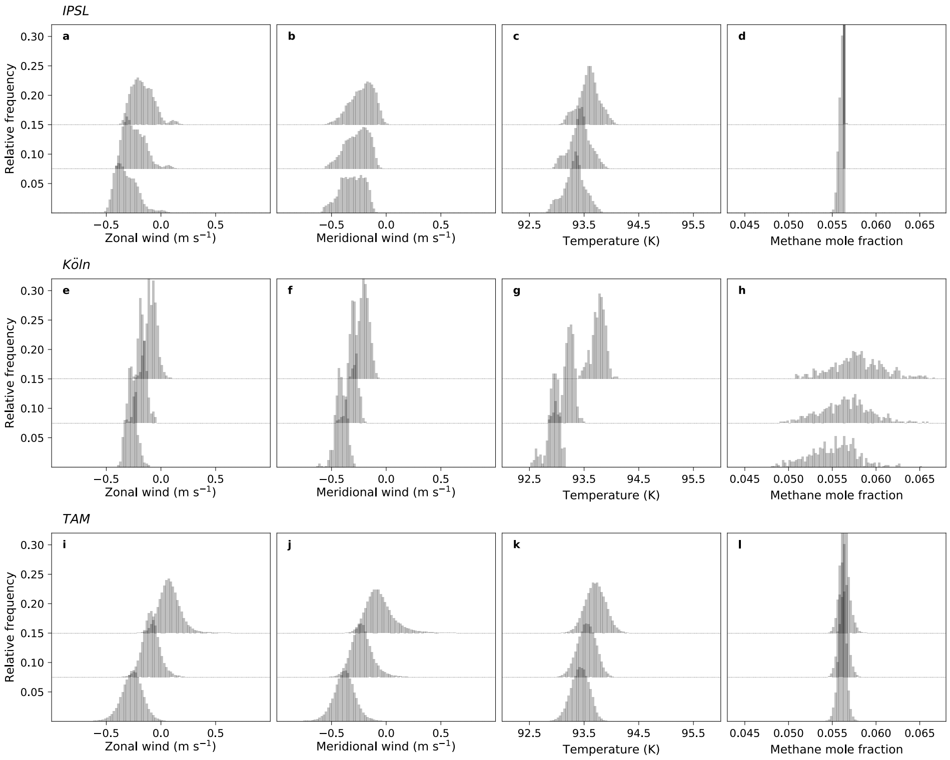

Figure 6: As in Fig. 5, but for the northern hemisphere (around 10°N).

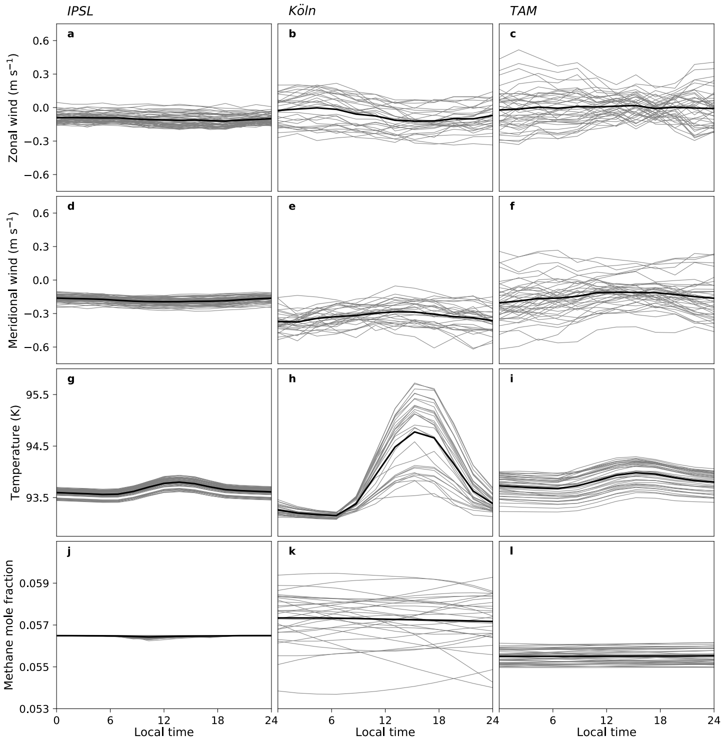

Figure 7: Diurnal variations (rows from top to bottom) of 10 m zonal wind, 10 m meridional wind, surface temperature, and boundary layer methane mole fraction at one longitude (the sub-Saturn point) over a 10 Tsol simulation around $L_S \approx 305°$. Results are shown for all latitudes within 10° of the equator. Individual locations and days are shown in light gray curves, with the 10 Tsol and regional average shown in black. The columns show results for different models.

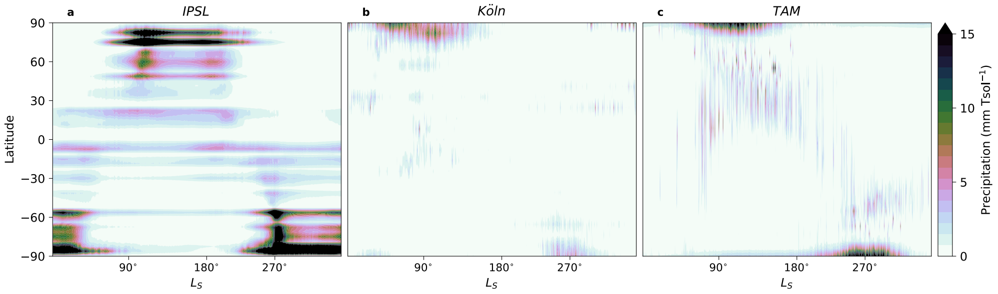

Figure 8: Zonal-mean climatological methane precipitation, starting from northern vernal equinox ($L_S = 0°$), as simulated by the different models.

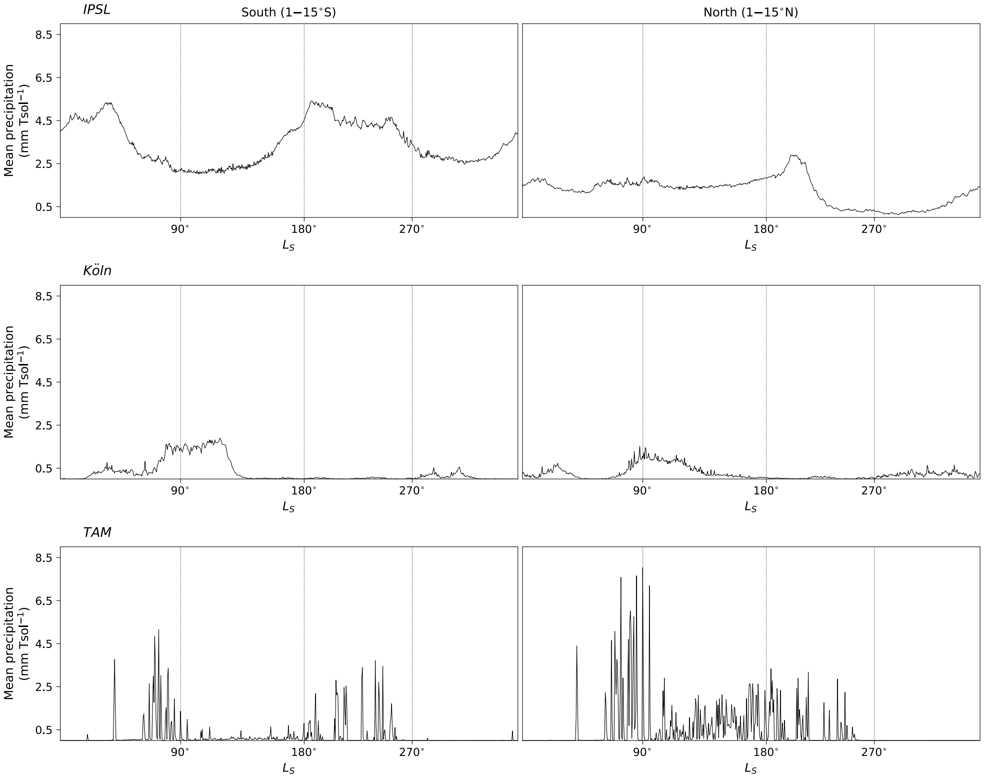

Figure 9: Time series of mean methane precipitation in the southern (left column) and northern (right column) low latitudes, starting from northern vernal equinox ($L_S = 0°$). The various rows show the results for different models.